Mechanics of human embryo compaction

Julie Firmin, Nicolas Ecker, Diane Rivet Danon, Özge Özgüç, Virginie Barraud Lange, Hervé Turlier, Catherine Patrat, Jean-Léon Maître

Article

Mechanics of human embryo compaction

https://doi.org/10.1038/s41586-024-07351-x

Received: 14 December 2021

Accepted: 26 March 2024

Published online: 01 May 2024

Check for updates

Julie Firmin[1,2,3], Nicolas Ecker[4], Diane Rivet Danon[3], Özge Özgüç[1], Virginie Barraud Lange[3,5], Hervé Turlier[4], Catherine Patrat[3,5] & Jean-Léon Maître[1]✉

The shaping of human embryos begins with compaction, during which cells come into close contact[1,2]. Assisted reproductive technology studies indicate that human embryos fail compaction primarily because of defective adhesion[3,4]. On the basis of our current understanding of animal morphogenesis[5,6], other morphogenetic engines, such as cell contractility, could be involved in shaping human embryos. However, the molecular, cellular and physical mechanisms driving human embryo morphogenesis remain uncharacterized. Using micropipette aspiration on human embryos donated to research, we have mapped cell surface tensions during compaction. This shows a fourfold increase of tension at the cell–medium interface whereas cell–cell contacts keep a steady tension. Therefore, increased tension at the cell–medium interface drives human embryo compaction, which is qualitatively similar to compaction in mouse embryos[7]. Further comparison between human and mouse shows qualitatively similar but quantitively different mechanical strategies, with human embryos being mechanically least efficient. Inhibition of cell contractility and cell–cell adhesion in human embryos shows that, whereas both cellular processes are required for compaction, only contractility controls the surface tensions responsible for compaction. Cell contractility and cell–cell adhesion exhibit distinct mechanical signatures when faulty. Analysing the mechanical signature of naturally failing embryos, we find evidence that non-compacting or partially compacting embryos containing excluded cells have defective contractility. Together, our study shows that an evolutionarily conserved increase in cell contractility is required to generate the forces driving the first morphogenetic movement shaping the human body.

The mechanical characterization of model organisms, including mammals, has immensely advanced our understanding of animal morphogenesis[5,6]. For ethical and technical reasons, human embryos are mostly inaccessible to experimentation. Therefore, our appreciation of how the human body shapes itself during embryonic development rarely comes from studies on human embryos themselves but instead relies mostly on the extrapolation from findings in other species and, more recently, from engineered human embryo models[8,9]. For example, we still do not know whether contractility of the actomyosin cortex, a major morphogenetic engine during animal development[5,6,10], plays a similarly important role during human morphogenesis[1]. Opportunely, pre-implantation development constitutes a unique setting to carry out experimentations on live embryos and can provide both validation and breakthrough in our understanding of human embryonic development[11–14].

Human morphogenesis begins with compaction on the fourth day after fertilization, when the embryo is composed of 8 to 16 cells[1–3,15]. After in vitro fertilization (IVF) during assisted reproductive technology (ART), embryos failing to compact entirely or with a delayed compaction show lower implantation rate on transfer[16–18], illustrating the importance of this process for further development. Also, human embryos can compact partially, with individual cells being excluded from the compacted mass[3,4]. However, the mechanisms leading to compaction failure in human embryos are unknown.

During compaction, cells maximize their cell–cell contact area and minimize their surface exposed to the outside medium[19]. This is akin to the adhesion of soap bubbles resulting from the balance of tensions at their interfaces. Following this analogy, we consider the surface tensions γ_{cc} and γ_{cm} at cell–cell contacts and at cell–medium interfaces, respectively, whose ratio determines the shape of contacts between cells as described previously[7,20]. Compaction of human embryos results from reducing a compaction parameter $\alpha = \cos(\theta_e/2) = \gamma_{cc}/2\gamma_{cm}$, where θ_e is the external contact angle between cells (Supplementary Note and Fig. 1a). Using time-lapse microscopy and micropipette aspiration, we have determined the contact angles and surface tensions of human embryos (Fig. 1a–d, Extended Data Fig. 1 and Supplementary Video 1). Taking the last observed third cleavage as a temporal landmark, we synchronized embryos to calculate average behaviours which recapitulates the trends of individual embryos (Extended Data Fig. 1a–e). We measured the growth of external contact angles θ_e from 81 ± 5° to 158 ± 4° in about 30 h (mean ± s.e.m. of 147 measurements on ten embryos, Student's t-test $P < 10^{-11}$; Fig. 1c and Supplementary Table 1). Concomitantly, surface tensions γ_{cm} increase from 0.62 ± 0.04 to 2.35 ± 0.08 nN µm^{-1} (mean ± s.e.m. of 147 measurements on ten embryos, Student's t-test

[1]Institut Curie, Université PSL, CNRS UMR3215, INSERM U934, Paris, France. [2]Université de Paris, Paris, France. [3]Service de Biologie de la Reproduction - CECOS, Paris Centre Hospital, APHP centre, FHU Prema, Paris, France. [4]Center for Interdisciplinary Research in Biology, Collège de France, CNRS, INSERM, Université PSL, FHU Prema, Paris, France. [5]Institut Cochin, Université de Paris, CNRS UMR1016, Paris, France. ✉e-mail: jean-leon.maitre@curie.fr

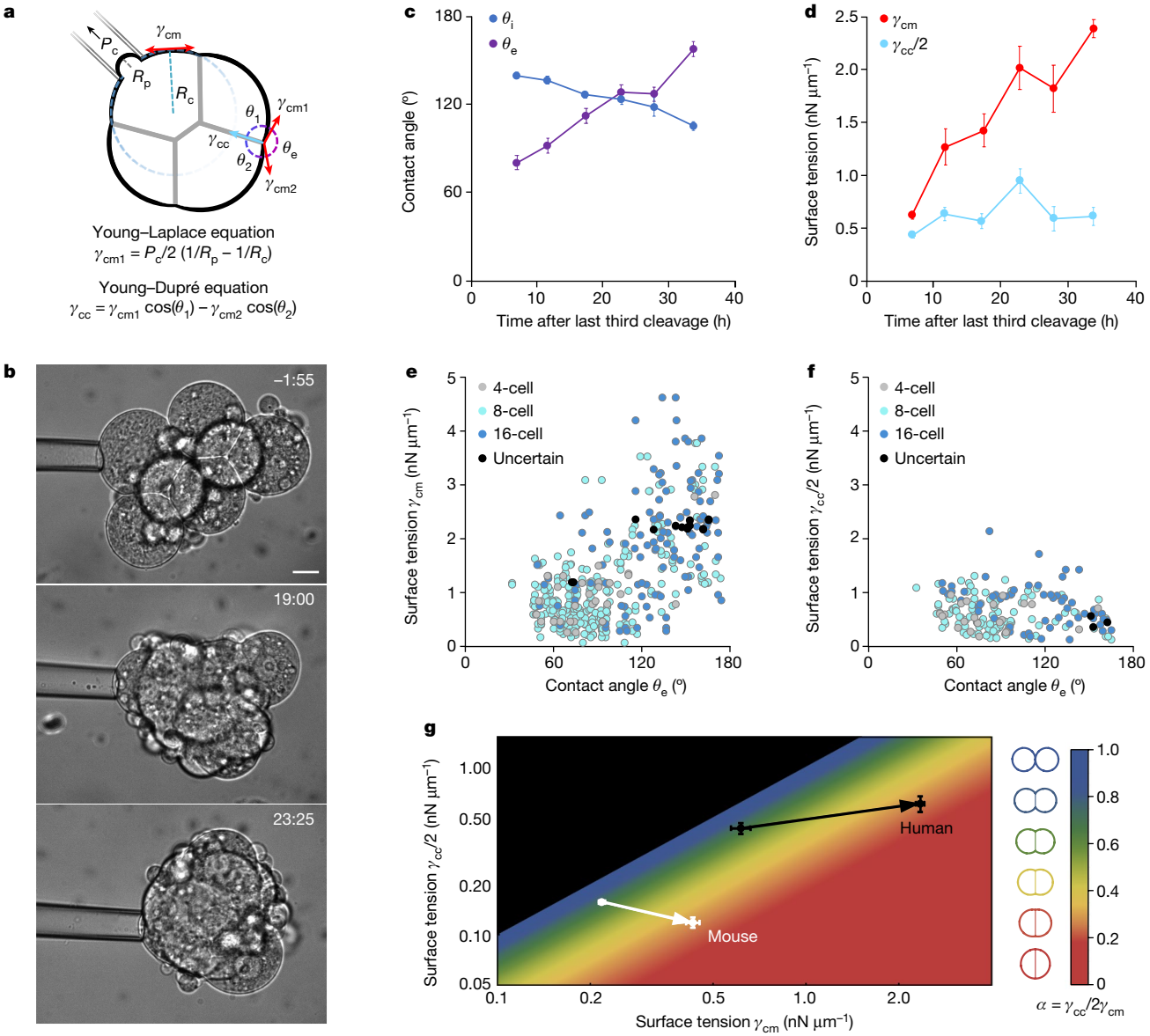

Fig. 1 | Spatiotemporal map of tensions during human embryo compaction. **a**, Diagram of surface tension mapping. Using a micropipette of radius R_p, a pressure P_c is applied to the surface of blastomeres of curvature $1/R_c$. The surface tension γ_{cm} is calculated using the Young–Laplace equation. From γ_{cm}, the external and internal contact angles (θ_e and θ_i and θ_2, respectively) of adjacent cells, the Young–Dupré equation yields the interfacial tension γ_{cc}. **b**, Representative images of a human embryo during micropipette aspiration shown in Supplementary Video 1. Time relative to last observed third cleavage division as hh:mm. Scale bar, 20 µm. **c**,**d**, Time course of internal and external contact angles θ_i and θ_e, respectively (**c**) and surface tensions γ_{cm} and $\gamma_{cc}/2$ (**d**). Mean ± s.e.m. calculated over bins of 5 h on a total of 147 blastomeres and 96 contacts from ten embryos synchronized to the time of last observed third cleavage division. Internal contact angles θ_i correspond to the average of the measured θ_1 and θ_2. Statistics can be found in Supplementary Table 1 and Source Data Fig. 1. **e**,**f**, Surface tension γ_{cm} (**e**) and $\gamma_{cc}/2$ (**f**) as a function of contact angles θ_e measured on 429 blastomeres from 14 embryos. Pearson correlation $R = 0.624$ for γ_{cm} and $R = -0.135$ for γ_{cc}. Cleavage stages are indicated with 4-, 8- and 16-cell stage blastomeres in grey, light and dark blue, respectively. Black dots show blastomeres that cannot reliably be staged. **g**, Phase diagram showing the state of compaction as a function of γ_{cm} and $\gamma_{cc}/2$ in log–log scale (Supplementary Note). Mean ± s.e.m. of data from human embryos are shown as a black arrow starting at 5–10 and ending at 30–35 h after the last third cleavage (30 and 5 cells, respectively). Mean ± s.e.m. of data from mouse embryos adapted from ref. 7 are shown as a white arrow starting at 0–2 and ending at 8–10 h after the third cleavage (112 and 36 cells, respectively). The compaction parameter $\alpha = \gamma_{cc}/2\gamma_{cm}$ is colour-coded on the right, with diagrams of the corresponding cell doublet shapes.

$P < 10^{-5}$) whereas surface tensions at cell–cell contacts $\gamma_{cc}/2$ remained steady at about 0.6 nN µm^{-1} (Fig. 1d and Supplementary Table 1). Independently of embryo synchronization, calculating the correlation between contact angles and surface tensions yields 0.740 for γ_{cm} and 0.028 for γ_{cc} over the entire duration of the experiments (44 measurement sessions on 14 embryos and Pearson correlation P values $<10^{-8}$ and $>10^{-1}$, respectively; Extended Data Fig. 1f,g). Therefore, the mechanical changes driving compaction are located at the cell–medium interface (Fig. 1 and Extended Data Fig. 1).

As cleavage divisions of blastomeres in individual embryos can occur hours apart from one another, compaction takes place with neighbouring cells at different cleavage stages (Fig. 1e,f and Supplementary Video 1). Tracking cleavage stages, surface tensions and contact angles shows that the mechanical changes associated with compaction can begin during the 8-cell stage and proceed as blastomeres undergo their fourth cleavage (Fig. 1e,f and Extended Data Fig. 2). This is delayed compared to the mouse, in which the mechanical changes driving a compaction of similar magnitude occur during the 8-cell stage[7]. However,

compaction in human embryos does not seem to depend on the volume reduction associated with cleavage divisions (Extended Data Fig. 3), as observed in mouse embryos[7]. Because of the relationship between cell curvature and surface tension, this implies that cell pressure increases during compaction, as measured experimentally (Extended Data Fig. 3). Further comparison between mouse and human shows that the increase in surface tension γ_{cm} during compaction is qualitatively conserved (Fig. 1g). However, although mouse embryos double their surface tension γ_{cm} (from about 0.2 to 0.4 nN μm^{-1}), human embryos increase it fourfold to drive contact angle changes of identical magnitude[7] (Fig. 1g, Extended Data Fig. 1 and Supplementary Note). In addition to increasing γ_{cm}, compaction in mouse embryos also relies on decreasing tensions at cell–cell contacts[7] (from about 0.15 to 0.10 nN μm^{-1} for $\gamma_{cc}/2$; Fig. 1g). We had previously calculated that, in the mouse, changes in tension γ_{cm} contributed to three-quarters of compaction and changes in tension γ_{cc} to one-quarter[7]. This is not the case in human embryos, which do not relax their cell–cell contacts and rely exclusively on the increase in tension γ_{cm} at the cell–medium interface (Fig. 1g). Therefore, mouse and human embryos share qualitatively conserved mechanisms but quantitatively different strategies to achieve the same morphogenesis. In the parameter space (γ_{cm}, $\gamma_{cc}/2$) used to plot the phase diagram shown in Fig. 1g, we can consider the minimal changes in surface tension required to compact as the shortest mean-squared distance between initial and compacted states. Interestingly, the strategy adopted by human embryos seems less efficient than the one of the mouse (Supplementary Note). Indeed, with growing external contact angles, any further increase in tension γ_{cm} becomes less and less effective as a result of cells pulling increasingly perpendicularly to the plane of cell–cell contacts[7,19]. Therefore, compared to the mouse, human embryos must generate considerable surface stresses (Fig. 1g) with potential implications for human embryo development such as cell fragmentation[21].

In mouse embryos, the increase in tension γ_{cm} is mediated by the actomyosin cortex[7], which tension depends on the architecture of the actin network and on the activity of myosin motors which determine the contractility of the network[22–24]. Furthermore, the reduction in tension γ_{cc} results in part from the downregulation of contractility, which requires signals from cadherin adhesion molecules[25]. To investigate the molecular and cellular regulation of the mechanics of human embryo compaction, we analysed the subcellular distribution of elements of the actomyosin cortex and cell–cell adhesion machinery which are most prominent during pre-implantation development[7,24,26]: non-muscle myosin 2 heavy chain paralogues MYH9 and MYH10, E-cadherin (CDH1), as well as filamentous actin (F-actin). We found that, as contact angles grow, the ratio between intensities at the cell–cell contacts and cell–medium interfaces decreases both for MYH10 and the phosphorylated form of MYH9 (pMYH9), whereas it remains stable for F-actin and CDH1 (Fig. 2a,b). This could result from pMYH9 and MYH10 cortical enrichment and/or from depletion at cell–cell contacts. Similarly to mouse embryos[7], this re-organization of myosin levels is compatible with increased contractility at the cell–medium interface, underlying raising tension γ_{cm} and steady cell–cell contacts, associated with stable γ_{cc} in human embryos (Fig. 1d).

To test whether contractility is responsible for generating the tensions driving human embryo compaction, we used ML7, an inhibitor of the myosin light chain kinase, on compacted embryos. ML7 caused embryos to decompact with contact angles dropping by 27 ± 2° within minutes (mean ± s.e.m. from six embryos, pairwise Student's *t*-test $P < 10^{-4}$; Fig. 2c–e and Supplementary Table 2). Concomitantly, we measured a threefold decrease in tension γ_{cm} between embryos in control and ML7-containing media (pairwise Student's *t*-test $P < 10^{-2}$; Fig. 2d and Supplementary Table 2). Notably, placing embryos back in regular medium allowed embryos to compact again (six of six embryos; Extended Data Fig. 4a,b) and to form a blastocyst (five of six embryos). This indicates that contractility is required for generating γ_{cm}, as in mouse embryos[7]. Therefore, contractility is an evolutionarily conserved engine generating the tension γ_{cm} driving compaction of both human and mouse embryos. Unlike the embryo which increases tension specifically at the cell–medium interface during compaction, ML7 inhibits contractility globally at both the cell–medium and cell–cell interfaces. On ML7 treatment, the tension at cell–cell contacts γ_{cc} also decreases to half the original value (pairwise Student's *t*-test $P < 10^{-3}$; Fig. 2e and Supplementary Table 2), indicating high levels of contractility acting at cell–cell contacts of human embryos. This would be different from what has been reported in mouse embryos, which show minimal contractility at their cell–cell contacts[7]. Because reducing γ_{cc} promotes compaction, high levels of contractility at cell–cell contacts also explain why global inhibition of contractility shows milder effects on compaction in human embryos as compared to mouse ones. Furthermore, high levels of contractility at cell–cell contacts could explain why human embryos increase their tension γ_{cm} twice as much as mouse ones to compact. This hints at differences in cellular behaviours between mouse and human embryos which would underlie different mechanical strategies driving compaction.

Despite lacking obvious molecular re-organization during compaction (Fig. 2a,b), cadherin-based cell–cell adhesion remains the prime suspect for compaction defects observed in ART[2–4,15,27]. Therefore, we decided to investigate the influence of cadherin-based adhesion onto surface tension in human embryos. Because cadherin adhesion molecules require Ca^{2+} to function[25], we placed compacted embryos in medium without Ca^{2+} and supplemented with EDTA (Fig. 2f). As previously observed[28], EDTA medium led to rapid decompaction of human embryos with contact angles dropping by 53 ± 8° (mean ± s.e.m. from six embryos, pairwise Student's *t*-test $P < 10^{-2}$; Fig. 2g,h and Supplementary Table 2), indicating that cadherin-based adhesion is required for compaction. As for contractility inhibition, placing embryos back into regular medium allowed embryos to compact again (six of six embryos; Extended Data Fig. 4c,d) and to form a blastocyst (four of six embryos). Surface tension measurements showed that tension γ_{cm} was not affected by EDTA medium whereas tension γ_{cc} increased twofold (pairwise Student's *t*-test $P > 10^{-1}$ and $P < 10^{-2}$, respectively; Fig. 2g,h and Supplementary Table 2). Therefore, as observed in mouse embryos[7], the tension γ_{cm} driving compaction is generated independently from cell adhesion, in a cell-autonomous manner. Embryos lacking adhesion decompact as a result of increased tension γ_{cc}. This might result from the direct loss of adhesion energy provided by the binding of cadherin adhesion molecules. However, adhesion energy was reported to be negligible during contact remodelling in several settings[25,29–31]. Alternatively, increased tension γ_{cc} is more likely to be the consequence of contractility at cell–cell contacts, as observed in the mouse[7].

Together, we find that, whereas both cell contractility and cell–cell adhesion are required for compaction of human embryos (Fig. 2c–h), only contractility reorganizes during compaction and generates the tension γ_{cm} which drives compaction (Fig. 2a,b). Therefore, human embryo compaction relies on contractility increasing surface tension specifically at the cell–medium interface, which constitutes molecular, cellular and mechanical mechanisms which are qualitatively conserved with the mouse embryo.

Loss of contractility and adhesion results in distinct mechanical signatures (Fig. 2i): low γ_{cm} and γ_{cc} with ML7 medium in contrast to high γ_{cm} and γ_{cc} with EDTA medium. Therefore, mechanical signatures could be used to distinguish which cellular process fails when compaction is defective[1,32].

To determine the mechanical origin of compaction defects, we measured the tensions of embryos spontaneously failing compaction. We considered that compaction failed when no contact angle would grow above 132°, as determined statistically from seven compacting and seven non-compacting embryos[33]. For these embryos, 30 h after the third cleavage and despite cells undergoing their fourth cleavage similarly to compacting embryos (Extended Data Fig. 2), mean contact angles kept steady below about 80° (Fig. 3a,b and Supplementary

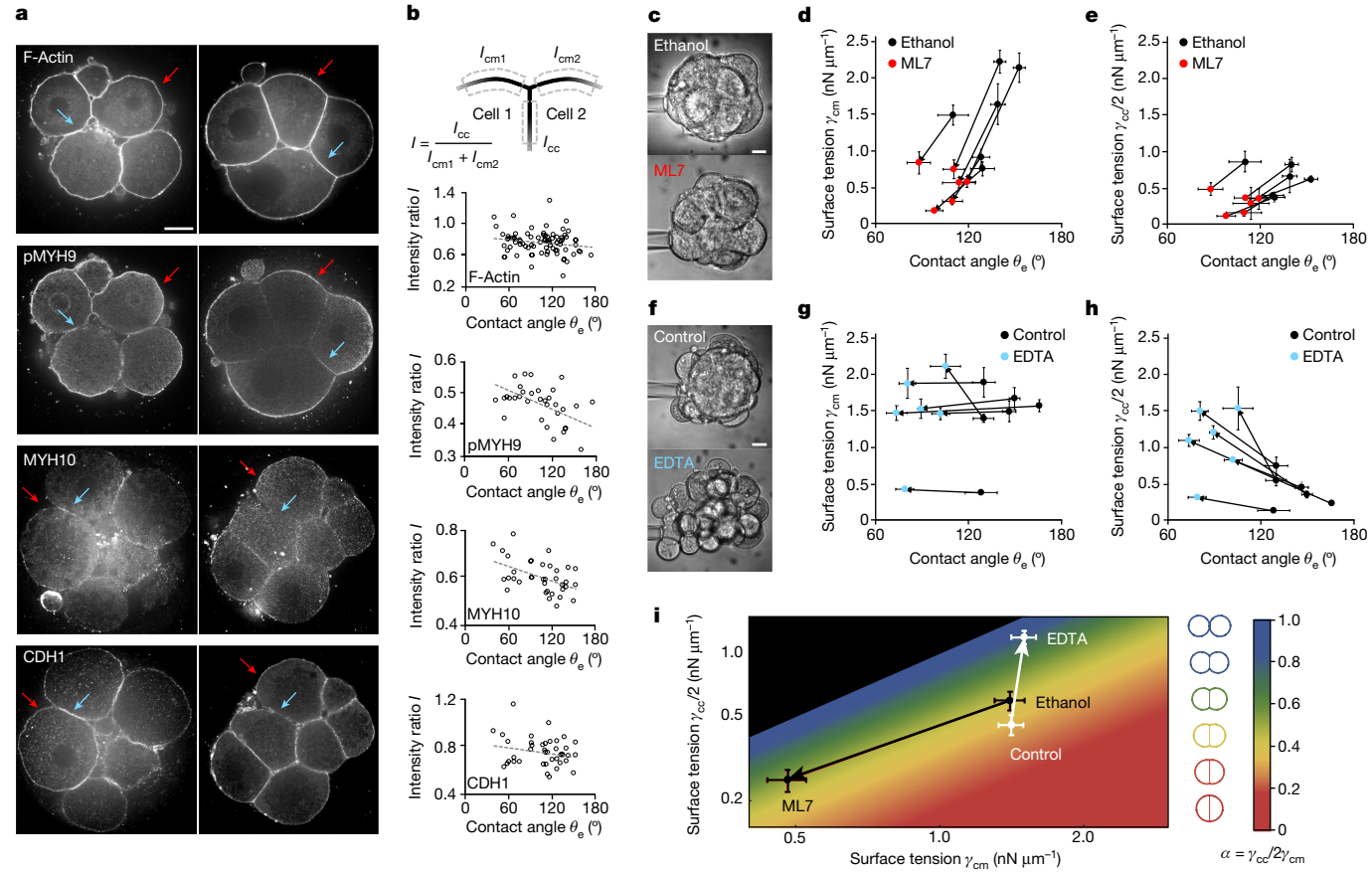

Fig. 2 | Role of cell contractility and cell adhesion in regulating tensions during human embryo compaction. a, Representative images of immunostaining of F-Actin, pMYH9, MYH10 and CDH1 on human embryos before (left) and after (right) compaction. Blue arrows point at cell–cell contacts and red arrows at cell–medium interfaces. Scale bar, 20 µm. **b**, Intensity ratio between the cell–cell and cell–medium interfaces as a function of the external contact angle θ_e. Pearson correlations $R = -0.181$ for F-actin (80 contacts from 21 embryos, $P > 10^{-2}$), −0.496 for pMYH9 (35 contacts from 11 embryos, $P < 10^{-2}$), −0.480 for MYH10 (36 contacts from nine embryos, $P < 10^{-2}$) and −0.217 for CDH1 (41 contacts from ten embryos, $P > 10^{-1}$). *P* values obtained from two-tailed Pearson correlation tests; Source Data Fig. 2. **c**, Representative images of embryos placed in medium containing 1:2,000 ethanol (top) and 10 µM ML7 (bottom) during micropipette aspiration. Scale bar, 20 µm. **d**,**e**, Surface tensions γ_{cm} (**d**) or γ_{cc} (**e**) as a function of external contact angles θ_e. Mean ± s.e.m. measured on 115 blastomeres from six embryos placed in ethanol (black) and ML7 (red) media. Comparisons between ethanol and ML7 media using two-tailed pairwise Student's *t*-test give $P < 10^{-4}$ for θ_e, $P < 10^{-2}$ for γ_{cm} and $P < 10^{-3}$ for $\gamma_{cc}/2$. Statistics in Supplementary Table 2; Source Data Fig. 2. **f**, Representative images of embryos placed in control medium (top) and EDTA (bottom) media during micropipette aspiration. Scale bar, 20 µm. **g**,**h**, Surface tensions γ_{cm} (**g**) or $\gamma_{cc}/2$ (**h**) as a function of external contact angles θ_e. Mean ± s.e.m. measured on 98 blastomeres from six embryos placed in normal (black) and EDTA (blue) media. Comparisons between control and EDTA media using two-tailed pairwise Student's *t*-test give $P < 10^{-2}$ for θ_e, $P > 10^{-1}$ for γ_{cm} and $P < 10^{-2}$ for $\gamma_{cc}/2$. Statistics in Supplementary Table 2; Source Data Fig. 2. **i**, Phase diagram showing the state of compaction as a function of γ_{cm} and $\gamma_{cc}/2$ in log–log scale (Supplementary Note). Mean ± s.e.m. of data from embryos transferred from ethanol to ML7 media (black, 55 and 60 cells from six embryos) or from control to EDTA media (white, 49 and 49 cells from six embryos). The compaction parameter $\alpha = \gamma_{cc}/2\gamma_{cm}$ is colour-coded on the right, with diagrams of the corresponding cell doublet shapes.

Table 3). Meanwhile, both tensions γ_{cm} and γ_{cc} remained low (Fig. 3b–d and Supplementary Table 3). This corresponds to the mechanical signature of defective contractility (Fig. 2i), indicating that all of the seven spontaneously failing embryos we have measured were unsuccessful in growing their contractility. Therefore, defective contractility could be a common cause of compaction failure in human embryos. As observed in mutant mouse embryos[7], if both contractility and adhesion were defective, we would also expect low tensions, which would be indistinguishable from faulty contractility alone. Therefore, in addition to contractility, adhesion might also be deficient in the embryos we have measured.

Another compaction defect that is commonly observed is partial compaction, in which some of the blastomeres do not participate in the compacted mass[1,3,4]. Such excluded cells are thought to be either eliminated from the blastocyst or could participate to extra-embryonic tissues such as the trophectoderm that forms at the surface of the embryo[1,2,34]. Biopsy of excluded cells suggests that those are more likely to be aneuploid, which led to the interesting hypothesis that compaction would serve as a way to eliminate aneuploid cells from embryonic tissues[4]. Furthermore, clonal analyses on human placenta from natural pregnancies found that aneuploid clones originate from blastomeres which had segregated into the trophectoderm during pre-implantation development[34]. This further supports the idea that human pre-implantation embryos eliminate aneuploid cells from embryonic tissues. However, how defective cells would be eliminated from the compacting morula is unknown.

To investigate this mechanism, we measured the tension of embryos showing partial compaction (Fig. 3e). We considered cells as excluded when they failed to raise their contact angle θ_e above 111° whereas the rest of the embryo compacted, as determined statistically from seven embryos containing one or more excluded cells[33]. In the same embryo, compacting blastomeres showed increasing contact angles θ_e and tensions γ_{cm}, whereas contact tensions γ_{cc} would remain steady, as described above (Figs. 1d and 3f and Supplementary Table 4).

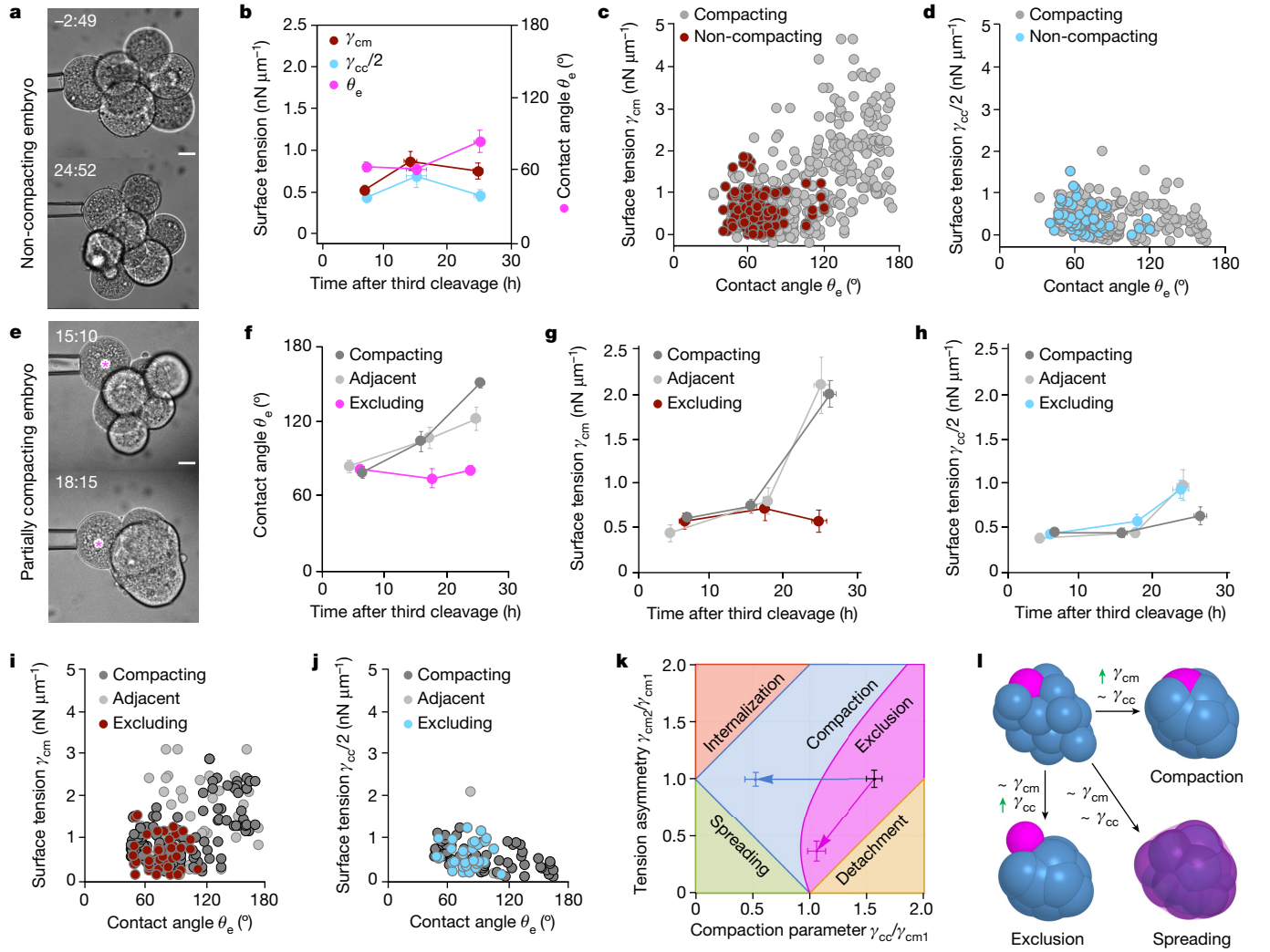

Fig. 3 | Mechanical signature of human embryos failing compaction. **a**, Representative images of embryos failing compaction with no contact reaching 132° for more than 30 h after the third cleavage. Time relative to last observed third cleavage division as hh:mm. Scale bar, 20 µm. Supplementary Video 2. **b**, Time course of contact angles θ_e (pink) and surface tensions γ_{cm} (dark red) and $\gamma_{cc}/2$ (blue). Mean ± s.e.m. calculated over bins of 10 h on a total of 38 blastomeres and 21 contacts from five non-compacting embryos synchronized to the time of last observed third cleavage division. Statistics can be found in Supplementary Table 3 and Source Data Fig. 3. **c**,**d**, Surface tension γ_{cm} (**c**) and $\gamma_{cc}/2$ (**d**) as a function of contact angles θ_e measured on 117 blastomeres from seven non-compacting embryos. Data from compacting embryos from Fig. 1e,f shown in grey. **e**, Representative images of a blastomere (labelled with pink asterisk) becoming excluded during compaction with contact angles <111° in compacting embryos with contact growing above 132° for more than 30 h after the third cleavage. Time relative to last observed third cleavage division as hh:mm. Scale bar, 20 µm. Supplementary Video 3. **f**–**h**, Time course of external contact angles θ_e (**f**) and surface tensions γ_{cm} (**g**) and $\gamma_{cc}/2$ (**h**) of excluding (pink, dark red and blue) blastomeres. Compacting blastomeres are shown in light grey if directly adjacent to an excluding blastomere and dark grey otherwise. Mean ± s.e.m. calculated over bins of 10 h on a total of 84 blastomeres and 101 contacts from five embryos synchronized to the time of last observed third cleavage division. Statistics in Supplementary Table 4 and Source Data Fig. 3. **i**,**j**, Surface tension γ_{cm} (**i**) and $\gamma_{cc}/2$ (**j**) as a function of external contact angles θ_e measured on 221 blastomeres from seven partially compacted embryos. Data from excluding blastomeres in dark red (**i**) and blue (**j**). Compacting blastomeres are shown in light grey if directly adjacent to an excluding blastomere and dark grey otherwise. **k**, Phase diagram showing the behaviours of a cell as a function of its tension γ_{cm2} or γ_{cc} normalized to the tension γ_{cm1} of the neighbouring cells composing the rest of the embryo (Supplementary Note). The ratio γ_{cc}/γ_{cm1} is analogous to the compaction parameter[7] shown in Figs. 1g and 2i. The ratio $\gamma_{cm2}/\gamma_{cm1}$ is analogous to the tension asymmetry discussed previously[35]. Mean ± s.e.m. of data from compacting (blue, six pairs of cells from five embryos) or excluding blastomeres (pink, five pairs of cells from five embryos) taken from Fig. 3i,j when partially compacting embryos reach the threshold contact angle of 132°. **l**, Simulations of compaction with distinct cell populations: blue blastomeres grow their tension γ_{cm} by a factor 3.2 and their tension γ_{cc} by 1.2 according to measurements shown in Fig. 3i,j; purple blastomeres do the same as blue ones (top right), keep γ_{cm} steady and grow their tension γ_{cc} by 1.2 (bottom right) or keep γ_{cm} steady and grow their tension γ_{cc} by 2.4 (bottom left). Supplementary Video 4.

Meanwhile, non-compacting blastomeres kept their contact angles θ_e and tension γ_{cm} low, ending up excluded from the compacted morula with minimal attachment (Fig. 3f–j and Supplementary Table 4). Thus, non-compacting blastomeres seem to lack contractility, similarly to embryos failing compaction entirely (Fig. 3b,c). Furthermore, the sorting out of non-compacting cells based on differences in tension γ_{cm} is reminiscent of the mechanism driving the positioning of low γ_{cm} trophectoderm progenitors and high γ_{cm} inner cell mass progenitors in the mouse embryo[35]. However, contrary to cells with low tensions γ_{cm} which sort out to the surface to become trophectoderm cells, excluded cells do not spread at the surface and instead keep minimal attachment (Fig. 3e). To understand how cells could become excluded, we developed a foam-like model describing the three-dimensional shape of contacting cells with different surface tensions at fixed volume (Extended Data Fig. 3 and Supplementary Note). The model produces the different expected configurations taken by cells in the embryo:

compacted, excluded, detached, internalized and spread (Fig. 3k and Supplementary Note). To illustrate this, we considered the outcome of different scenarios of surface tension changes using numerical simulations (Supplementary Note)[35]. Using measured values of γ_{cm} and γ_{cc} faithfully recapitulated normal compaction in silico (Fig. 3k,l and Supplementary Video 4). To consider cell exclusion, we maintained γ_{cm} at its initial levels in one cell, while changing γ_{cm} normally in neighbouring cells as measured experimentally (Fig. 3g). When both γ_{cm} and γ_{cc} were maintained low, we did not observe exclusion but noted instead the spreading of the weak cell (Fig. 3k,l and Supplementary Video 4). On the other hand, increasing γ_{cc} led to cell exclusion (Fig. 3k,l and Supplementary Video 4), as observed experimentally. Therefore, exclusion requires γ_{cc} to increase (Fig. 3k,l). Indeed, unlike for compacting cells, we measured a twofold increase in γ_{cc} between excluded cells and their compacting neighbour (from 0.42 ± 0.05 to 0.91 ± 0.10 nN µm^{-1} for $\gamma_{cc}/2$ in five embryos, mean ± s.e.m., Student's t-test $P < 10^{-2}$; Fig. 3h and Supplementary Table 4). This increase could arise from high contractility at cell–cell contacts from both or from only one of the contacting cells. Because our measurements of γ_{cm} suggest that excluded cells have low contractility, high γ_{cc} is more likely to originate from the contractility of the neighbouring non-excluded cells (Fig. 3j). Increased contractility specifically at this interface would constitute an active mechanism by which cells from human embryos would recognize and eliminate unfit cells. Investigating the presence of such mechanism will benefit from the rich literature on cell competition reported in model organisms[36].

Together, using the mechanical signatures of human pre-implantation embryos[32], we can provide a more accurate explanation for compaction defects which are commonly observed in ART studies[4,17]. Moreover, this first study on the mechanics of human embryonic morphogenesis shows that normal compaction results from an evolutionarily conserved increase in cell contractility at the cell–medium interface (Figs. 1 and 2). Although qualitatively conserved, the force patterns driving the same morphogenetic movement in mouse and human are quantitively different, with human embryos being less mechanically efficient than mouse ones (Fig. 1g and Supplementary Note). Therefore, we show that the same morphogenesis does not necessarily rely on identical force patterns, which is reminiscent of developmental system drift reported for signalling modules[37]. We think this illustrates how studying the evolution of morphogenesis immensely benefits from our ability to measure mechanical properties of embryos in ways that allow comparison[38], ideally directly with a physical unit[39]. This will be key to discovering how physical laws are leveraged by nature to produce the breathtaking diversity of the shapes of life.

Online content

Any methods, additional references, Nature Portfolio reporting summaries, source data, extended data, supplementary information, acknowledgements, peer review information; details of author contributions and competing interests; and statements of data and code availability are available at https://doi.org/10.1038/s41586-024-07351-x.

1. Firmin, J. & Maître, J.-L. Morphogenesis of the human preimplantation embryo: bringing mechanics to the clinics. *Semin. Cell Dev. Biol.* **120**, 22–31 (2021).
2. Shahbazi, M. N. Mechanisms of human embryo development: from cell fate to tissue shape and back. *Development* **147**, dev190629 (2020).
3. Coticchio, G., Lagalla, C., Sturmey, R., Pennetta, F. & Borini, A. The enigmatic morula: mechanisms of development, cell fate determination, self-correction and implications for ART. *Hum. Reprod. Update* **25**, 422–438 (2019).
4. Lagalla, C. et al. Embryos with morphokinetic abnormalities may develop into euploid blastocysts. *Reprod. BioMed. Online* **34**, 137–146 (2017).
5. Collinet, C. & Lecuit, T. Programmed and self-organized flow of information during morphogenesis. *Nat. Rev. Mol. Cell Biol.* **22**, 245–265 (2021).
6. Heisenberg, C.-P. & Bellaïche, Y. Forces in tissue morphogenesis and patterning. *Cell* **153**, 948–962 (2013).
7. Maître, J.-L., Niwayama, R., Turlier, H., Nédélec, F. & Hiiragi, T. Pulsatile cell-autonomous contractility drives compaction in the mouse embryo. *Nat. Cell Biol.* **17**, 849–855 (2015).
8. Haniffa, M. et al. A roadmap for the Human Developmental Cell Atlas. *Nature* **597**, 196–205 (2021).
9. Rossant, J. & Tam, P. P. L. Opportunities and challenges with stem cell-based embryo models. *Stem Cell Rep.* **16**, 1031–1038 (2021).
10. Özgüç, Ö. & Maître, J.-L. Multiscale morphogenesis of the mouse blastocyst by actomyosin contractility. *Curr. Opin. Cell Biol.* **66**, 123–129 (2020).
11. Fogarty, N. M. E. et al. Genome editing reveals a role for OCT4 in human embryogenesis. *Nature* **550**, 67–73 (2017).
12. Gerri, C. et al. Initiation of a conserved trophectoderm program in human, cow and mouse embryos. *Nature* **587**, 443–447 (2020).
13. Okamoto, I. et al. Eutherian mammals use diverse strategies to initiate X-chromosome inactivation during development. *Nature* **472**, 370–374 (2011).
14. Petropoulos, S. et al. Single-cell RNA-seq reveals lineage and X chromosome dynamics in human preimplantation embryos. *Cell* **165**, 1012–1026 (2016).
15. Iwata, K. et al. Analysis of compaction initiation in human embryos by using time-lapse cinematography. *J. Assist. Reprod. Genet.* **31**, 421–426 (2014).
16. Coticchio, G. et al. Perturbations of morphogenesis at the compaction stage affect blastocyst implantation and live birth rates. *Hum. Reprod.* **36**, 918–928 (2021).
17. Rienzi, L. et al. Time of morulation and trophectoderm quality are predictors of a live birth after euploid blastocyst transfer: a multicenter study. *Fertil. Steril.* **112**, 1080–1093 (2019).
18. Skiadas, C., Jackson, K. & Racowsky, C. Early compaction on day 3 may be associated with increased implantation potential. *Fertil. Steril.* **86**, 1386–1391 (2006).
19. Turlier, H. & Maître, J.-L. Mechanics of tissue compaction. *Semin. Cell Dev. Biol.* **47–48**, 110–117 (2015).
20. Goel, N. S., Doggenweiler, C. F. & Thompson, R. L. Simulation of cellular compaction and internalization in mammalian embryo development as driven by minimization of surface energy. *Bull. Math. Biol.* **48**, 167–187 (1986).
21. Pelzer, D. et al. Cell fragmentation in mouse preimplantation embryos induced by ectopic activation of the polar body extrusion pathway. *EMBO J.* **42**, e114415 (2023).
22. Chugh, P. et al. Actin cortex architecture regulates cell surface tension. *Nat. Cell Biol.* **19**, 689–697 (2017).
23. Özgüç, Ö. et al. Cortical softening elicits zygotic contractility during mouse preimplantation development. *PLoS Biol.* **20**, e3001593 (2022).
24. Schliffka, M. F. et al. Multiscale analysis of single and double maternal-zygotic Myh9 and Myh10 mutants during mouse preimplantation development. *eLife* **10**, e68536 (2021).
25. Maître, J.-L. & Heisenberg, C.-P. Three functions of cadherins in cell adhesion. *Curr. Biol.* **23**, R626–R633 (2013).
26. Yan, L. et al. Single-cell RNA-seq profiling of human preimplantation embryos and embryonic stem cells. *Nat. Struct. Mol. Biol.* **20**, 1131–1139 (2013).
27. Wamaitha, S. E. & Niakan, K. K. Human pre-gastrulation development. *Curr. Top. Dev. Biol.* **128**, 295–338 (2018).
28. Zakharova, E. E., Zaletova, V. V. & Krivokharchenko, A. S. Biopsy of human morula-stage embryos: outcome of 215 IVF/ICSI cycles with PGS. *PLoS ONE* **9**, e106433 (2014).
29. Maitre, J.-L. et al. Adhesion functions in cell sorting by mechanically coupling the cortices of adhering cells. *Science* **338**, 253–256 (2012).
30. Chan, E. H., Chavadimane Shivakumar, P., Clément, R., Laugier, E. & Lenne, P.-F. Patterned cortical tension mediated by N-cadherin controls cell geometric order in the *Drosophila* eye. *eLife* **6**, e22796 (2017).
31. Stirbat, T. V. et al. Fine tuning of tissues' viscosity and surface tension through contractility suggests a new role for α-catenin. *PLoS ONE* **8**, e52554 (2013).
32. Guck, J. Some thoughts on the future of cell mechanics. *Biophys. Rev.* **11**, 667–670 (2019).
33. Budczies, J. et al. Cutoff Finder: a comprehensive and straightforward web application enabling rapid biomarker cutoff optimization. *PLoS ONE* **7**, e51862 (2012).
34. Coorens, T. H. H. et al. Inherent mosaicism and extensive mutation of human placentas. *Nature* **592**, 80–85 (2021).
35. Maître, J.-L. et al. Asymmetric division of contractile domains couples cell positioning and fate specification. *Nature* **536**, 344–348 (2016).
36. Matamoro-Vidal, A. & Levayer, R. Multiple influences of mechanical forces on cell competition. *Curr. Biol.* **29**, R762–R774 (2019).
37. True, J. R. & Haag, E. S. Developmental system drift and flexibility in evolutionary trajectories. *Evol. Dev.* **3**, 109–119 (2001).
38. Ichbiah, S., Delbary, F., McDougall, A. & Dumollard, R. Embryo mechanics cartography: inference of 3D force atlases from fluorescence microscopy. *Nat. Methods* **20**, 1989–1999 (2023).
39. Lenne, P.-F. et al. Roadmap for the multiscale coupling of biochemical and mechanical signals during development. *Phys. Biol.* **18**, 041501 (2021).

Methods

Ethics statement

The use of human embryos donated for this project was allowed by the Agence de la Biomédecine (approval no. RE 17-011 R) in compliance with the International Society for Stem Cell Research (ISSCR) guidelines[40]. All human pre-implantation embryos used were donated after patients had fulfilled all reproductive needs. Informed written consent was obtained from both patients of all couples who donated embryos following IVF treatment. No financial incentives were offered for the donation.

Donated embryos were cryopreserved and stored at Fertilité Paris Centre ART Center (Biologie de la reproduction-CECOS, Cochin, APHP. Centre-Université de Paris), Clinique La Muette (Paris, France) or Clinique Pierre Chérest (Neuilly sur Seine, France). Embryos were then transferred to the Institut Curie where they were immediately thawed and used for the research project.

Patients and embryos

A total of 54 embryos provided by 40 couples have been used for this study. Embryos were frozen on day 2 ($n = 33$) or day 3 ($n = 21$) according to slow freezing procedure ($n = 41$) or vitrification ($n = 13$). The mean cell number, at frozen time, was 4 ± 1 cells (mean ± s.d., minimum 2 and maximum 9 cells) and 8 ± 1 cells (mean ± s.d., minimum 4 and maximum 10 cells) for day 2 and day 3 frozen embryos, respectively. For measurements throughout compaction (Figs. 1 and 3), day 2 embryos were thawed. For measurements on compacted embryos (Fig. 2c–i) both day 2 and day 3 embryos were thawed. For immunostained embryos (Fig. 2a,b), day 3 embryos were thawed.

Embryos were frozen for 12.2 ± 5.1 yr (mean ± s.d., 12.2 ± 5.1 and 5.7 ± 1.1 yr for slow-freeze and vitrified embryos, respectively).

The donors mean ages were 33.5 ± 3.7 and 35.0 ± 7.2-year-old for female and male patients, respectively (mean ± s.d., data available for 35 of the 40 couples, data at present missing for 5 couples). A total of 34/52 embryos were generated by intracytoplasmic sperm injection and 18/52 embryos were conceived using classical IVF (data missing for 2/54 embryos coming from 1/40 couple). All sperm were fresh.

Embryo work

Thawing. Embryos were handled using Stripper micropipettes (Origio) on binoculars (Leica M80) equipped with heating plates (Leica MATS-Type TL base) set to 37 °C when needed.

Cryopreserved embryos were thawed according to manufacturer's instructions. Embryo thawing packs (Origio) were used for slow-freeze embryos. Vit Kit (Irvine Scientific) was used for vitrified embryos. The intact survival rate, defined as the percentage of embryos without any cell lysis immediately after thawing, was 89% (48/54) for the embryos further considered for experimentation. All embryos survived the warming process with at least 50% of intact cells.

Culture. Embryos were handled using Stripper micropipettes (Origio) on binoculars (Leica M80) equipped with heating plates (Leica MATS-Type TL base) set to 37 °C. Embryos are placed in pre-equilibrated (at least 4 h at 37 °C, 5% O_2, 5% CO_2) CSCM-C medium (Irvine Scientific) covered with mineral oil (Irvine Scientific) in 50 mm glass bottom dishes (MatTek Corporation P50G-1,5-30-F) in an incubator (New Brunswick Galaxy 48 R) or the incubation chamber of the microscopes (Leica DMI6000 B with custom incubation from EMBLEM or Zeiss CellDiscoverer 7 with a 37 °C humidified atmosphere supplemented with 5% CO_2 and depleted to 5% O_2 by supplementing N_2).

Zona pellucida dissection. Before surface tension measurements, embryos were dissected out of their zona pellucidae on the day of their thawing using a holding pipette and a glass needle[41].

The holding pipette and needle were custom-made from glass capillaries (Harvard apparatus, GC100TF-15) pulled using a P-97 Flaming Brown needle puller (Sutter Instrument) with the following settings: ramp +25, pull 65, velocity 80, time 175 and pressure 200. To forge the holding pipette, the glass needle was cut to about 120 µm diameter using a microforge (Narishige, MF-900) and the tip was fire-polished to about 20 µm inner diameter. To forge the needle, the tip was melted onto the glass bead and pulled back to obtain a solid pointed tip. Both needle and pipette were bent to a 20° degrees angle to be parallel to the dish surface when mounted on the micromanipulator (Leica, AM6000). The holding pipette can apply controlled pressures using mineral oil-filled tubing coupled to a piston of which the position is moved using a microscale translating stage (Eppendorf, CellTram Oil 5176).

Chemical reagents. ML7 (Sigma-Aldrich, I2764) was diluted in 50% ethanol to 10 mM. Day 4 compacted embryos were placed into medium containing 1:2,000 ethanol for 15 min before surface tension measurements for an extra 30 min. Embryos were then moved into medium containing 10 µM ML7 for 15 min before surface tension measurements taking another 30 min. Embryos were then placed back into normal culture medium CSCM-C to recover. Six of six embryos recompacted and five of six embryos formed a blastocyst.

Similarly, day 4 compacted embryos were placed into Embryo Biopsie Medium (Irvine Scientific), a commercial medium without Ca^{2+} and supplemented with 0.5 mM EDTA for 10 min before surface tension measurements taking another 20 min. Embryos were then placed back into normal culture medium CSCM to recover. Six of six embryos recompacted and four of six embryos formed a blastocyst.

Immunostaining

Embryos were fixed in 2% PFA (Euromedex, 2000-C) for 10 min at 37 °C, washed in PBS and permeabilized in 0.01% Triton X-100 (Euromedex, T8787) in PBS (PBT) at room temperature before being placed in blocking solution (PBT with 3% BSA) at 4 °C for at least 4 h. Primary antibodies (Supplementary Table 5) were applied in blocking solution at 4 °C overnight. After washes in PBT at room temperature, embryos were incubated with secondary antibodies, DAPI and phalloidin at room temperature for 1 h (Supplementary Table 6). Embryos were washed in PBT and imaged immediately after in PBS with BSA under mineral oil.

Micropipette aspiration

Micropipette preparation. To forge the micropipettes, glass capillaries (World Precision Instruments TW100-3) were pulled using a P-97 Flaming Brown needle puller (Sutter Instrument) with the following settings: ramp +3–5, pull 55, velocity 50, time 50 and pressure 500.

Using a microforge (Narishige, MF-900), needles were cut to form a blunt opening of radius 12–22 µm and bent 80–100 µm away from the tip at a 20° angle.

Micro-aspiration setup. The micropipette was mounted on a micromanipulator (Leica AM6000) using a grip head and capillary holder (Eppendorf, 920007392 and 9200077414). The micropipette was connected to a PBS-filled intermediate reservoir of which the height is controlled using a 50 mm microscale translating stage (Newport) to generate positive and negative pressures[42]. The intermediate reservoir was connected to a microfluidic pump (Fluigent, MFCS-EZ) delivering negative pressures with a 2.5 Pa resolution. The pressure is controlled using Maesflow software (Fluigent). The output pressure was calibrated by finding the height of the intermediate reservoir at which no flow in the micropipette is observed (using floating particles found in the dish, 'no flow' is considered achieved when the position of the particle inside the micropipette is stable for about 10 s and if slow drift can be reverted with 10 Pa).

Surface tension and pressure measurement. To measure cell surface tension, the micropipette was brought in contact with the free surface of a blastomere of an embryo with a low grabbing pressure (20–30 Pa; Fig. 1a). The pressure was then increased stepwise (10 Pa steps) until the deformation of the blastomeres reaches the radius of the micropipette (R_p). At steady state, the surface tension γ_{cm} of the blastomeres was calculated using Young–Laplace's law: $\gamma_{cm} = P_c/2(1/R_p - 1/R_c)$, where P_c is the pressure used to deform the cell of radius R_c. The pressure was then released and relaxation of the deformation was observed. Pressure increments are applied after 20–50 s, depending on how close the deformation is to a hemisphere. It typically took 3–5 min to probe a cell. In a measurement session, four to ten cells are measured in a given embryo, depending on its number of cells. Some cells are measured several times throughout compaction.

To calculate cells hydrostatic pressure P, we use once again the Young–Laplace's law: $P = 2\gamma_{cm}/R_c$.

Interfacial tension measurement. After measuring the surface tension of two adjacent cells of the embryo, we assumed steady state on the timescale of the measurement and calculate the interfacial tension from the force balance equation at the cell–cell contact (Fig. 1a). On the basis of the general Young–Dupré equation, we calculated $\gamma_{cc} = -\gamma_{cm1}\cos(\theta_1) - \gamma_{cm2}\cos(\theta_2)$, where γ_{cm1} and γ_{cm2} are the surface tensions of cell 1 and 2, θ_1 and θ_2, the internal contact angles of cell 1 and 2 and γ_{cc} is the interfacial tension at the cell–cell contact. In the approximation of contacting cells with equivalent surface tensions γ_{cm}, the contribution of each blastomere to γ_{cc} is $\gamma_{cc}/2$ (ref. 7).

Microscopy

Pipette-scope. Surface tension measurements were performed on a Leica DMI6000 B inverted microscope equipped with a ×40/0.8 DRY HC PL APO Ph2 (11506383) objective operated by Metamorph 7.10.4.407. A ×0.7 lens is mounted in front of a Retina R3 camera. The microscope is equipped with a custom incubation chamber (EMBLEM) to keep the sample at 37 °C and maintain the atmosphere at 5% CO_2 and 5% O_2.

Time-lapse imaging. For time-lapse imaging, embryos were placed after thawing in the chamber of a CellDiscoverer 7 (Zeiss) humidified 37 °C, 5% O_2, 5% CO_2 atmosphere operated by Zen 3.6.095.09000. Embryos were imaged every 30 min at five to eight focal planes separated by 10 µm using IR-LED (725 nm) transmitted light through a ×20/0.95 objective. Images were acquired using either an ORCA-Flash 4.0 camera (Hamamatsu, C11440) or a 506 axiovert (Zeiss) camera.

Spinning disc microscope. Immunostainings were imaged on a Zeiss Observer Z1 microscope with a CSU-X1 spinning disc unit (Yokogawa) using 405, 488, 561 and 642 nm laser lines through a ×63/1.2 C Apo Korr water immersion objective; emission was collected through 450/50 nm, 525/50 nm, 595/50 band pass or 610 nm low pass filters onto an ORCA-Flash 4.0 camera (C11440, Hamamatsu) operated by Metamorph 7.10.4.407.

Data analyses

Image analysis. Pipette size, cell radii of curvature, contact angles were measured using Fiji with the line, circle and angle tools, respectively[43]. In brief, the equatorial plane of the object is taken to manually draw a line between the inner walls of the pipette or a circle fitting the cell–medium interface of cells. To measure external contact angles, two line segments are drawn tangentially to the cell–medium interfaces of two contacting cells with their intersection located at the cell–cell contact edge (Fig. 1a). Similarly, to measure internal contact angles, two line segments are drawn: one along the cell–cell contact and another tangentially to the cell–medium interface of one of the contacting cells (Fig. 1a). As an internal control of the measurement, we verify that the three angles roughly sum up to 360° (with a tolerance of 10°).

To measure cortical intensity, as done previously[7], we picked confocal slices cutting through the equatorial plane of two contacting cells using Fiji. We drew a 1 µm thick line along the cell–medium interface or cell–cell contact, measured the mean intensity and divided the contact intensity by the sum of the cell–medium intensities of contacting cells.

To measure the volume of cells, we use Bitplane Imaris to draw the contour of cells along the F-actin signal on confocal slices of stained embryos, as done previously[7].

Statistics. Mean, s.d., s.e.m. and Pearson's correlation coefficients, were calculated using Excel (Microsoft). Statistical tests were performed with the free online tool BiostaTGV (https://biostatgv.sentiweb.fr/), based on R. Two-tailed and pairwise Student's *t*-tests and Pearson's correlation tests were performed when needed. Statistical significance was considered when $P < 10^{-2}$.

The ten embryos shown in Fig. 1c,d were averaged by bins of 5 h after the time of last observed third cleavage. The resulting mean trends recapitulate the one observed in representative embryos (Fig. 1 and Extended Data Fig. 1). The five embryos shown in Fig. 3b and five embryos shown in Fig. 3f,h were averaged by bins of 10 h after the time of last observed third cleavage. Each embryo had been characterized throughout two to five measurement sessions, which could begin before the last observed third cleavage. Therefore, all embryos are not included in each bin group.

Contact angle thresholds were determined using Cutoff Finder[33], a bundle of optimization and visualization methods for cutoff determination based on R (https://molpathoheidelberg.shinyapps.io/CutoffFinder_v1/).

Non-compacting embryos and fully compacting embryos were qualitatively assessed according to ESHRE guidelines[44]. Only non-compacting embryos in which cell divisions could be observed were considered. On the basis of seven fully compacting embryos and seven non-compacting embryos, maximizing specificity (100%) for detecting non-compacting embryos gave a sensitivity of 82% and a cutoff angle at 132° with an area under the curve (AUC) of 0.995. For partially compacting embryos, qualitative assessment of 14 excluded cells in seven partially compacting embryos, following recent descriptions of the phenomenon[4,16], yielded a cutoff angle of 111° found with 100% specificity, 81% sensitivity and AUC of 0.93. Data of fully compacting embryos are included in Fig. 1 and Extended Data Figs. 1–3. Data of non-compacting embryos are included in Fig. 3b–d and Extended Data Fig. 2. Data of partially compacting embryos are included in Figs. 1 and 3f–k and Extended Data Figs. 1–3.

Volume threshold to classify cells as 8-cell stage and larger or 16-cell stage and smaller were also determined using Cutoff Finder[33]. We used embryos counting precisely 8 or 16 cells to set the size of 8- and 16-cell stage in Cutoff Finder, which yielded a threshold of 49,850 µm^3 with 91% specificity, 100% sensitivity and AUC of 0.99. Using this classification, we find 8-cell stage and larger blastomeres at 73,518 ± 20,341 µm^3 and 16-cell stage and smaller at 33,148 ± 7,352 µm^3 (mean ± s.e.m. of 83 and 54 cells, respectively).

The sample size was not predetermined and simply results from the repetition of experiments. No sample was excluded. No randomization method was used. The investigators were not blinded during experiments.

Reporting summary

Further information on research design is available in the Nature Portfolio Reporting Summary linked to this article.

Data availability

Images and data are available from the BioImage Archive under accession number S-BIAD915. Simulations of compaction using surface

tension values from experiments were used to illustrate different scenarios of surface tension changes. Source data are provided with this paper.

Code availability

Custom code is available at https://doi.org/10.5281/zenodo.10779533 (ref. 45).

40. Clark, A. T. et al. Human embryo research, stem cell-derived embryo models and in vitro gametogenesis: considerations leading to the revised ISSCR guidelines. *Stem Cell Rep.* **16**, 1416–1424 (2021).
41. Tsunoda, Y., Yasui, T., Nakamura, K., Uchida, T. & Sugie, T. Effect of cutting the zona pellucida on the pronuclear transplantation in the mouse. *J. Exp. Zool.* **240**, 119–125 (1986).
42. Guevorkian, K. & Maître, J.-L. Micropipette aspiration: a unique tool for exploring cell and tissue mechanics in vivo. *Methods Cell. Biol.* **139**, 187–201 (2017).
43. Schindelin, J. et al. Fiji: an open-source platform for biological-image analysis. *Nat. Methods* **9**, 676–682 (2012).
44. Alpha Scientists in Reproductive Medicine and ESHRE Special Interest Group of Embryology et al. The Istanbul consensus workshop on embryo assessment: proceedings of an expert meeting. *Hum. Reprod.* **26**, 1270–1283 (2011).
45. Ecker, N. & Turlier, H. 3D active foam simulations. Zenodo https://zenodo.org/doi/10.5281/zenodo.10779532 (2024).

Acknowledgements We thank the imaging platform of the Genetics and Developmental Biology unit at the Institut Curie (PICT-IBiSA@BDD), member of the French National Research Infrastructure France-BioImaging (ANR-10-INBS-04) for their outstanding support. We thank N. Kazdar, L. Delaroche and A. Le Dû and all the members of ART teams from the Clinique La Muette (Paris, France), the Clinique Pierre Chérest (Neuilly sur Seine, France) and the Hopital Cochin (Paris, France) for support with human embryo experiments. We thank all members of the Maître laboratory, Y. Bellaïche and M.-H. Verlhac for discussion and comments. We acknowledge the support with administrative issues from M.-H. Verlhac throughout this project. We are grateful to the patients who donated their surplus embryos to research. This project was funded by a Paris Sciences et Lettres (PSL) QLife (ANR-17-CONV-0005) grant to J.-L.M., C.P. and H.T. and the INSERM transversal programme Human Development Cell Atlas (HuDeCA) to J.-L.M. and C.P. Research in the laboratory of J.-L.M. is supported by the Institut Curie, the Centre National de la Recherche Scientifique (CNRS), the Institut National de la Santé Et de la Recherche Médicale (INSERM) and is funded by grants from the Fondation Schlumberger pour l'Éducation et la Recherche through the Fondation pour la Recherche Médicale, the European Molecular Biology Organization Young Investigator program (EMBO YIP), Labex DEEP (ANR- 11-LABX-0044, part of the IDEX PSL ANR-10-IDEX-0001–02). J.F. is funded by a fellowship from the Fondation pour la Recherche Médicale (FDM202006011290). The work by H.T. and N.E. was supported by the CNRS and Collège de France. No fund from the European Research Council was used for this project.

Author contributions J.F., H.T., C.P. and J.-L.M. conceptualized the project and acquired funding. J.F. and J.-L.M. designed experiments. J.F. performed experiments. J.F., Ö.Ö. and J.-L.M. analysed the data. J.F., D.R.D., V.B.L and C.P. organized embryo collection. N.E. and H.T. wrote the theory and performed numerical simulations. J.-L.M. wrote the manuscript with inputs from J.F., N.E., H.T. and C.P.

Competing interests The authors declare no competing interests.

Additional information

Supplementary information The online version contains supplementary material available at https://doi.org/10.1038/s41586-024-07351-x.

Correspondence and requests for materials should be addressed to Jean-Léon Maître.

Peer review information *Nature* thanks Berenika Plusa, Hilde Van de Velde, Alpha Yap and the other, anonymous, reviewer(s) for their contribution to the peer review of this work. Peer reviewer reports are available.

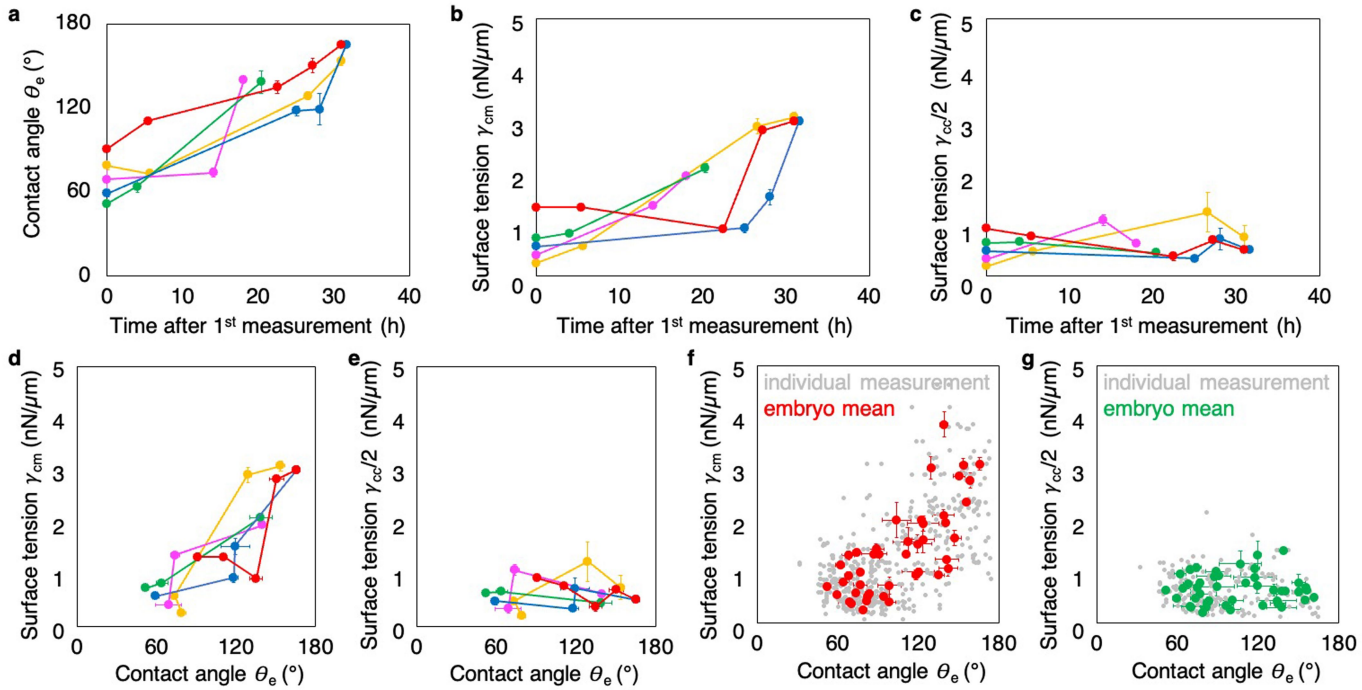

Extended Data Fig. 1 | Contact angle and surface tension measurements of individual embryos. (a-c) Time course of external contact angles θ_e (a) and surface tensions γ_{cm} (b) and $\gamma_{cc}/2$ (c) of 5 representative embryos. Time starts from the first tension measurement. Each embryo is measured in 3–5 sessions, for which the mean ± SEM of 2 to 12 contacting cells are shown. (d-e) Mean ± SEM surface tension γ_{cm} (d) and $\gamma_{cc}/2$ (e) as a function of contact angles θ_e over successive measurement session of 5 representative embryos. Each embryo is measured in 3–5 sessions, for which the mean ± SEM of 2 to 12 contacting cells are shown. (f-g) Surface tension γ_{cm} (f) and $\gamma_{cc}/2$ (g) as a function of contact angles θ_e measured on 429 blastomeres from 14 embryos. Individual measurements are shown in grey (Pearson correlation values $R = 0.624$ for γ_{cm} ($p < 10^{-47}$) and $R = -0.135$ for γ_{cc} ($p > 10^{-2}$)) and mean ± SEM of 44 individual measurement sessions on 14 embryos are shown in red for γ_{cm} (Pearson correlation values of $R = 0.740$ ($p < 10^{-8}$)) and in green for γ_{cc} $R = 0.028$ for γ_{cc} ($p > 10^{-1}$)). p values obtained from the 2-tailed Pearson correlation critical values table.

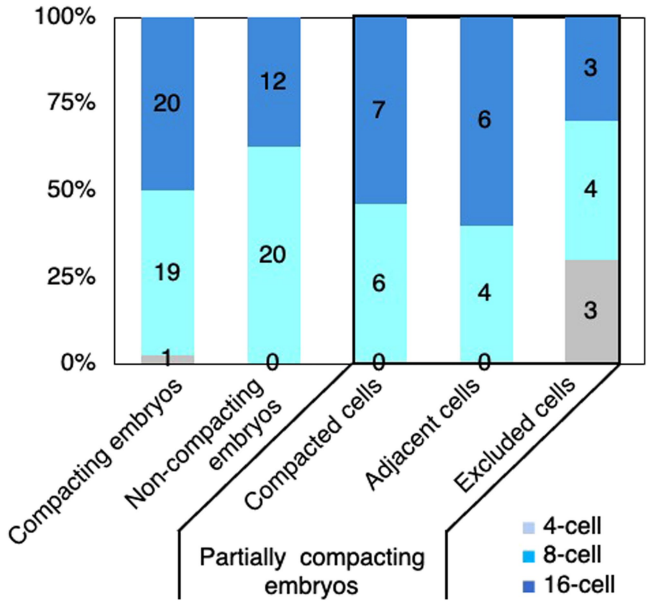

Extended Data Fig. 2 | Cleavage stage of compacting and non-compacting blastomeres. Blastomere stage, as determined by tracking successive cell divisions until the last tension measurement, of compacting, non-compacting and partially compacting embryos (7, 6 and 7 embryos and 40, 32 and 33 blastomeres respectively). For partially compacting embryos, the stages of compacted blastomeres, compacted blastomeres adjacent to excluded cells and excluded cells are indicated separately (13, 10 and 10 respectively).

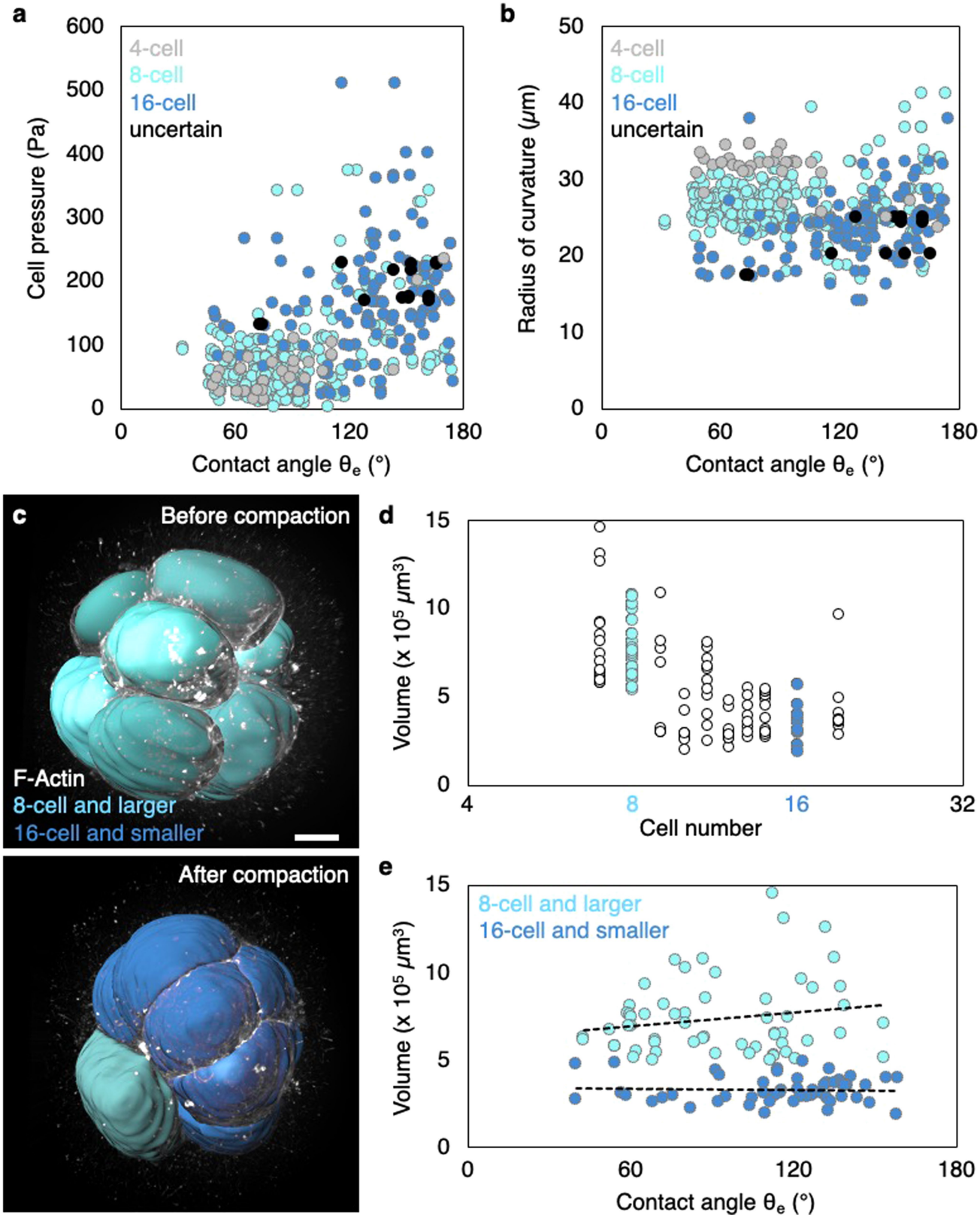

Extended Data Fig. 3 | See next page for caption.

Extended Data Fig. 3 | Volume and pressure changes during compaction. (a-b) Hydrostatic pressure (a) and radius of curvature (b) of cells as a function of contact angles θ_e measured on 429 blastomeres from 14 embryos. Cleavage stages are determined based on tracking divisions on time lapse microscopy and are indicated with 4-, 8- and 16-cell stage blastomeres in grey, light and dark blue respectively. Black dots show blastomeres that cannot be staged with certainty. Pearson correlation R = 0.551 for the hydrostatic pressure and −0.044 for the radius of curvature. (c) Volume segmentation of embryos before and after compaction. Cells are shown in light blue when estimated to be the size of a 8-cell stage blastomere and larger, or shown in dark blue when the size of a 16-cell stage blastomere and smaller. (d) Volume of segmented cells as a function of the total number of cells in the embryo (118 cells from 21 embryos). Embryos with precisely 8 or 16 cells are indicated in light or dark blue respectively. Embryos with precisely 8 or 16 cells are used to statistically determine the characteristic size of 8- and 16-cell stage blastomeres respectively. Using these measurements, a size threshold is statistically determined at 49850 μm^3 to classify cells as 8-cell stage blastomere and larger or 16-cell stage blastomere and smaller[33]. (e) Volume of 118 segmented cells as a function of the contact angle θ_e measured on 112 contacts from 21 embryos. Cells classified as 8-cell stage blastomere and larger are shown in light blue and cells classified as 16-cell stage blastomere and smaller are shown in dark blue. Pearson correlation between cell volume and contact angles are 0.176 for 8-cell stage blastomeres and larger (59 contacts, $p > 10^{-1}$) and −0.034 for 16-cell stage blastomeres and smaller (53 contacts, $p > 10^{-1}$). p values obtained from 2-tailed Pearson correlation tests.

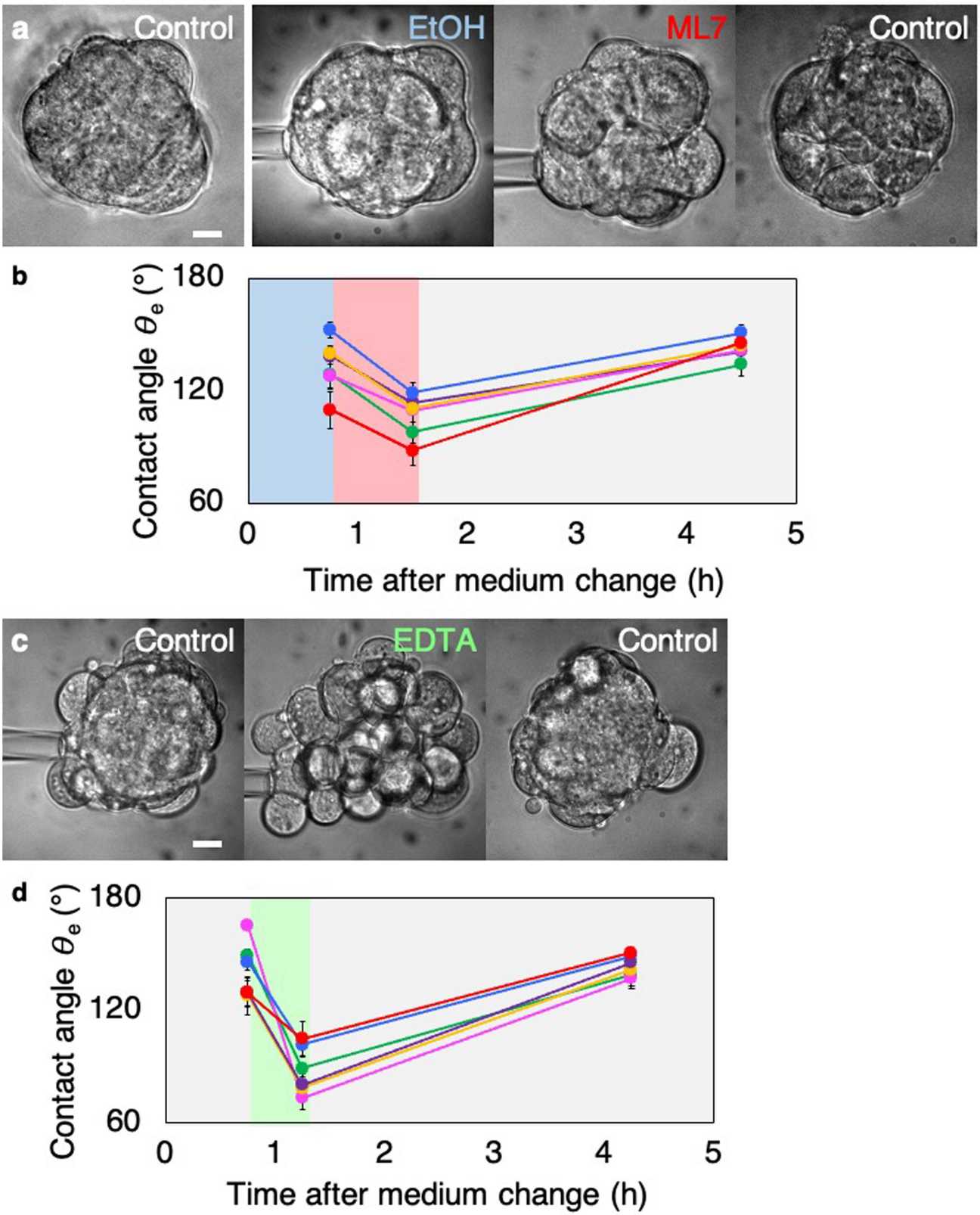

Extended Data Fig. 4 | Recovery of compaction after ML7 and EDTA media treatments. (a) Representative images of embryos in control medium (left) placed in medium containing 1:2000 ethanol (EtOH) for 45 min, then 10 µM ML7 for 45 min and after 3 h recovery in control medium (right). Scale bar, 20 µm. (b) Contact angles θ_e of embryos placed sequentially in control EtOH, ML7 and control media (Mean ± SEM of 59, 51, 44 contacts from 6 embryos). (c) Representative images of embryos placed in control medium (left) for 45 min, then EDTA containing medium for 30 min (center) and after 3 h recovery in control medium (right). Scale bar, 20 µm. (d) Contact angles θ_e of embryos placed sequentially in control, EDTA and control media (Mean ± SEM of 54, 43, 54 contacts from 6 embryos).

nature portfolio

Corresponding author(s): Jean-Léon Maître

Last updated by author(s): Mar 20, 2024

Reporting Summary

Nature Portfolio wishes to improve the reproducibility of the work that we publish. This form provides structure for consistency and transparency in reporting. For further information on Nature Portfolio policies, see our Editorial Policies and the Editorial Policy Checklist.

Statistics

For all statistical analyses, confirm that the following items are present in the figure legend, table legend, main text, or Methods section.

n/a	Confirmed
☐	☒ The exact sample size (*n*) for each experimental group/condition, given as a discrete number and unit of measurement
☐	☒ A statement on whether measurements were taken from distinct samples or whether the same sample was measured repeatedly
☐	☒ The statistical test(s) used AND whether they are one- or two-sided *Only common tests should be described solely by name; describe more complex techniques in the Methods section.*
☒	☐ A description of all covariates tested
☐	☒ A description of any assumptions or corrections, such as tests of normality and adjustment for multiple comparisons
☐	☒ A full description of the statistical parameters including central tendency (e.g. means) or other basic estimates (e.g. regression coefficient) AND variation (e.g. standard deviation) or associated estimates of uncertainty (e.g. confidence intervals)
☒	☐ For null hypothesis testing, the test statistic (e.g. *F*, *t*, *r*) with confidence intervals, effect sizes, degrees of freedom and *P* value noted *Give P values as exact values whenever suitable.*
☒	☐ For Bayesian analysis, information on the choice of priors and Markov chain Monte Carlo settings
☒	☐ For hierarchical and complex designs, identification of the appropriate level for tests and full reporting of outcomes
☒	☐ Estimates of effect sizes (e.g. Cohen's *d*, Pearson's *r*), indicating how they were calculated

Our web collection on statistics for biologists contains articles on many of the points above.

Software and code

Policy information about availability of computer code

Data collection	Images are acquired using Zeiss ZEN 3.6.095.09000 or Metamorph 7.10.4.407
Data analysis	Images are analysed using FIJI. Data and statistics are analysed using Microscoft Excel and R (via online tools BiostaTGV (https://biostatgv.sentiweb.fr/). Simulations of compaction using surface tension values from experiment were used to illustrate different scenarios of surface tension changes. Custom code is available at https://doi.org/10.5281/zenodo.10779533.

For manuscripts utilizing custom algorithms or software that are central to the research but not yet described in published literature, software must be made available to editors and reviewers. We strongly encourage code deposition in a community repository (e.g. GitHub). See the Nature Portfolio guidelines for submitting code & software for further information.

Data

Policy information about availability of data

All manuscripts must include a data availability statement. This statement should provide the following information, where applicable:

- Accession codes, unique identifiers, or web links for publicly available datasets
- A description of any restrictions on data availability
- For clinical datasets or third party data, please ensure that the statement adheres to our policy

All raw data and analyses used in the study are provided at https://www.ebi.ac.uk/biostudies/bioimages/studies/S-BIAD915

Research involving human participants, their data, or biological material

Policy information about studies with human participants or human data. See also policy information about sex, gender (identity/presentation), and sexual orientation and race, ethnicity and racism.

Reporting on sex and gender	Frozen embryos donated to research came from 40 couples of patients. The sex of the embryos was not determined.
Reporting on race, ethnicity, or other socially relevant groupings	Donors were couples who had received help conceiving with IVF in France. Race or ethnicity of the donors are unknown.
Population characteristics	The donors mean ages were 33.5 ± 3.7 and 35.0 ± 7.2 year-old for female and male patients respectively (mean ± SD, data available for 35 of the 40 couples, data currently missing for 5 couples).
Recruitment	All human preimplantation embryos used were donated after patients had fulfilled all reproductive needs. Informed written consent was obtained from both patients of all couples that donated embryos following IVF treatment. No financial incentive were offered for the donation.
Ethics oversight	The use of human embryos donated for this project was allowed by the Agence de la Biomédecine (ABM, approval number RE 17-011R) in compliance with the International Society for Stem Cell Research (ISSCR) guidelines.

Note that full information on the approval of the study protocol must also be provided in the manuscript.

Field-specific reporting

Please select the one below that is the best fit for your research. If you are not sure, read the appropriate sections before making your selection.

☒ Life sciences ☐ Behavioural & social sciences ☐ Ecological, evolutionary & environmental sciences

For a reference copy of the document with all sections, see nature.com/documents/nr-reporting-summary-flat.pdf

Life sciences study design

All studies must disclose on these points even when the disclosure is negative.

Sample size	When thawing human embryos, we cannot guess a priori the outcome of its development in general and of compaction in particular. The sample size was not predetermined and simply results from the repetition of experiments.
Data exclusions	No sample was excldued
Replication	All replication attempts were successful and each experiment was repeated in at least 3 technical repeats.
Randomization	No randomization method was used. When thawing human embryos, we cannot guess a priori the outcome of its development in general and of compaction in particular. In drug treatment experiments, compacted embryos were randomly allocated to control or drug treatments.
Blinding	The investigators were not blinded during the experiments. When thawing human embryos, we cannot guess a priori the outcome of its development in general and of compaction in particular.

Reporting for specific materials, systems and methods

We require information from authors about some types of materials, experimental systems and methods used in many studies. Here, indicate whether each material, system or method listed is relevant to your study. If you are not sure if a list item applies to your research, read the appropriate section before selecting a response.

Materials & experimental systems

n/a	Involved in the study
☐	☒ Antibodies
☒	☐ Eukaryotic cell lines
☒	☐ Palaeontology and archaeology
☒	☐ Animals and other organisms
☒	☐ Clinical data
☒	☐ Dual use research of concern
☒	☐ Plants

Methods

n/a	Involved in the study
☒	☐ ChIP-seq
☒	☐ Flow cytometry
☒	☐ MRI-based neuroimaging

Antibodies

Antibodies used

pMYH9 1:200 Cell Signaling Technology, 5026 AB_10576567
MYH10 1:200 Santa Cruz, sc-376942
CDH1 1:200 Cell Signaling Technology, 3195 AB_2291471
Alexa Fluor Plus 488 anti-mouse 1:200 Invitrogen, A32723 AB_2633275
Alexa Fluor 546 anti-mouse 1:200 Invitrogen, A11003 AB_2534071
Alexa Fluor Plus 488 anti-rabbit 1:200 Invitrogen, A32731 AB_2633280
Alexa Fluor Plus 546 anti-rabbit 1:200 Invitrogen, A11010 AB_2534077
Alexa Fluor 633 phalloidin 1:200 Invitrogen, A22284

Validation

Antibodies were validated by the manufacturer and were tested on mouse embryos by us.

Plants

Seed stocks

Report on the source of all seed stocks or other plant material used. If applicable, state the seed stock centre and catalogue number. If plant specimens were collected from the field, describe the collection location, date and sampling procedures.

Novel plant genotypes

Describe the methods by which all novel plant genotypes were produced. This includes those generated by transgenic approaches, gene editing, chemical/radiation-based mutagenesis and hybridization. For transgenic lines, describe the transformation method, the number of independent lines analyzed and the generation upon which experiments were performed. For gene-edited lines, describe the editor used, the endogenous sequence targeted for editing, the targeting guide RNA sequence (if applicable) and how the editor was applied.

Authentication

Describe any authentication procedures for each seed stock used or novel genotype generated. Describe any experiments used to assess the effect of a mutation and, where applicable, how potential secondary effects (e.g. second site T-DNA insertions, mosiacism, off-target gene editing) were examined.